Research article

Parametric evaluation of electrical discharge coatings on nickel-titanium shape memory alloy in deionized water

Ahmad Fairuz Mansor [a], Azwan Iskandar Azmi [a,*], Mohd Zahiruddin Md Zain [b], Roshalliza Jamaluddin [b]

[a] Faculty of Engineering Technology, Universiti Malaysia Perlis, UniCITI Alam Campus, 02100, Padang Besar, Perlis, Malaysia
[b] School of Manufacturing Engineering, Universiti Malaysia Perlis, Pauh Putra Campus, 02600, Pauh Perlis, Malaysia

A B S T R A C T

Nickel-titanium shape memory alloy (NiTi) has a unique capacity to restore its initial shape after deformation, which is highly applicable to orthopaedic implantations, especially for the minimization of invasive surgeries. The high nickel content of this alloy can lead to unfavourable effects on the human body upon dissolution; thus, a reliable barrier of coatings on the NiTi surface is required to alleviate the nickel migration and increase its biocompatibility. In this paper, analyses of a titanium oxide layer development on NiTi surface using electrical discharge coating (EDC) process is presented. The recast layer thickness, crater sizes, and surface roughness were characterized based on five parameters; polarity, discharge duration, pulse interval, peak current, and gap voltage. The results show that the discharge duration is the most significant parameter to influence all responses, followed by peak current. The surface characteristics of the EDC substrate is depending on the crater formations and is highly correlated with the discharge energy intensity. As a result, appropriate parametric conditions of the electrical discharge coating process can enhance the NiTi surface for future medical applications, without compromising the shape memory effect.

1. Introduction

Nickel-titanium (NiTi) shape memory alloy is an intermetallic material composed of approximately equi-atomic nickel and titanium elements. This alloy has superior properties of remarkable recoverable strain with respect to the induction of the shape memory effect and superelasticity, beside to its excellent mechanical properties. The shape memory effect refers to the capacity of the alloy to recover its original shape during the martensitic state after being heated beyond the austenite finish temperature [1]. Moreover, super-elasticity refers to the shape-recovery capacity under the application of an external force between the austenite start (A_s) and finish (A_f) temperatures, and this occurs without heat energy stimuli [2]. The alloy transforms to the detwinned martensite after loading, and it is abruptly reverted to the austenite state after unloading.

The NiTi alloy is extensively employed in the civil, aerospace, and biomedical fields. In biomedical applications, it is typically used as orthodontic arch wires, coronary stents, scoliosis correction rods, and bone fracture fixation devices. The shape memory properties of this alloy is

useable for the aforementioned applications in order to minimize invasive surgery [3, 4], increase the fixation of bone segments [5] and retain proper alignment of teeth [2] by its uniform compressive stress after the recovery. However, the effects of the corrosion and abrasion of this alloy have not been clarified. In general, nickel is not biocompatible material like titanium. The high nickel content of this alloy might reduce its biocompatibility and harmful for long-term of implantation. The release of nickel ions into human tissue is a dangerous cause that can trigger inflammatory reactions and carcinogens [6].

The presence of nickel reservoir in form of Ni_3Ti and pure nickel phase under the surface sublayer of the NiTi alloy will trigger continuous nickel release that increases the corrosion [7]. Besides, the smaller size of nickel atoms than that of titanium make them easily diffuse through an interstitial path and leach from the alloy surface. Under normal conditions, the NiTi alloy has a natural passivation of oxide film in the fluidic environment of human bodies, and most orthopaedic devices are dependent on its capacity to protect the implant surface. This film can act as a kinetic barrier towards corrosion and prevent metal ion transportation [8]. In the human body, the film is reliable for the depletion of

the nickel released at thicknesses of greater than 100 nm [9]. However, after a long period of implantation, the film damages due to mechanical stress or abrasion that induce the release of ions; thus resulting in the need for revision surgery, which is excessively expensive and may subject to a significant amount of pain. Hence, as an initial preventative measure, the surface modification of the NiTi alloy is required to sustain the biocompatibility of the alloy.

There are several suitable compositions for implant coatings such as TiN, TiC, TiCN, Al2O3, ZrO2, CaP, HA, and diamond [10]. Among these compositions, titanium oxide is required for bioactivity. This composition can induce apatite nucleation; thus allowing for the cell response and osteo-conductivity on the implant to be accelerated [11, 12]. Over several decades, several techniques have been proposed for the development of the biocompatible layer of titanium oxide on the NiTi alloy. However, most of the techniques only enhanced the native formation or passivation of the oxide film via oxidation treatment. These techniques include autoclaving and boiling baths [13], selective oxidation [14], sol-gel technology [15], and anodization in acid electrolytes [16], among other methods. In these studies, the nickel ion migration was minimized; however, the formed oxide layers were excessively thin and unable to withstand sufficiently long implantation periods. In order to overcome this limitation, alternative technique such as the electrical discharge process has been investigated by several researchers on biomaterials such as NiTi, Ti-6Al-4V, Ti–35Nb–7Ta–5Zrβ, and Ti-Ta alloys [17, 18, 19, 20, 21, 22]. Compared with the formation of the native oxide film generated by the abovementioned processes, the coating layer produced by the electrical discharge results in a high bonding strength, excellent wear and corrosion resistances, and significant biological activity [22]. The process allows for the preparation of a suitable surface for osseointegration due to nano-porous and multi features length from the microscale to nano-scale [11, 23].

The EDC process is a revolutionary technique, which is an adaptation of the electrical discharge machining (EDM) process. Moreover, it uses repetitive electrical pulses to generate heat energy on the workpiece surface within a temperature range of 8000–12 000 °C [24], which can melt and evaporate metal alloys into debris irrespective of their mechanical and thermo-physical properties. At the end of the erosion, the debris is flushed away from the machined area by dielectric fluid that flow in a high rate. On the other hand, a large portion of molten area re-solidify and remains on the machined surface. This leads to the formation of a significantly hard recast layer due to the quenching

phenomena in the dielectric fluid. The layer is composed of an inter-mixture of molten metals (workpiece and tool electrode) and dielectric compositions. The layer may not be unfavourable due to the defect generation, and it may limit certain applications. However, with appropriate parameters, the EDC process is a potential method for the realization of suitable material coatings for biomedical applications.

Similar to the EDM process, the EDC method is operated based on the generation of electrical pulses for the induction of sparking actions on a workpiece surface. Material erosion is essential for the development of the appropriate adhesion of the oxide layer composition. Figure 1 presents the schematic of electrical discharge pulses, which illustrates several critical EDC parameters such as the discharge duration, peak current, gap voltage, and pulse interval. With reference to the literature, the discharge duration and peak current have a significant influence on the material erosion process [25, 26, 27, 28]. Moreover, both parameters have a direct influence on the discharge energy, which is the main factor with respect to heat energy generation. The correlation of the parameters with the discharge energy was expressed by M. Kunieda, et al. [29], as expressed by the following Eq. (1):

$$q = u_e \; i_e \; t_e \tag{1}$$

where q = discharge energy, u_e = discharge voltage, i_e = discharge current, and t_e = discharge duration. The discharge voltage is uncontrolled; however, it is dependent on the electrode and workpiece materials, dielectric fluids, and process conditions. The functionalities of the gap voltage and pulse interval were described by S. Clijsters et al. [30]. The authors reported that the gap voltage is under the influence of the electrical potential in the dielectric fluids and induces an ionization path. In particular, an increase in the gap voltage can reduce the removal rate due to an increase in the gap distance. However, a decrease in this parameter within a short pulse interval can result in a short-circuit. Moreover, polarity is a critical parameter for the facilitation of the erosion target, to increase the material deposition on the substrate. Generally, material removal during EDM is from both workpiece and tool electrodes, and material removal rate is higher at electrode that is connected to positive polarity although both electrodes are made from the same material. However, it is depending on discharge duration and type of dielectric. When hydrocarbon oil is used, at sufficiently long discharge duration, dissociation of the dielectric will release carbon elements and they are attracted to the positive polarity and act as heat insulator at the
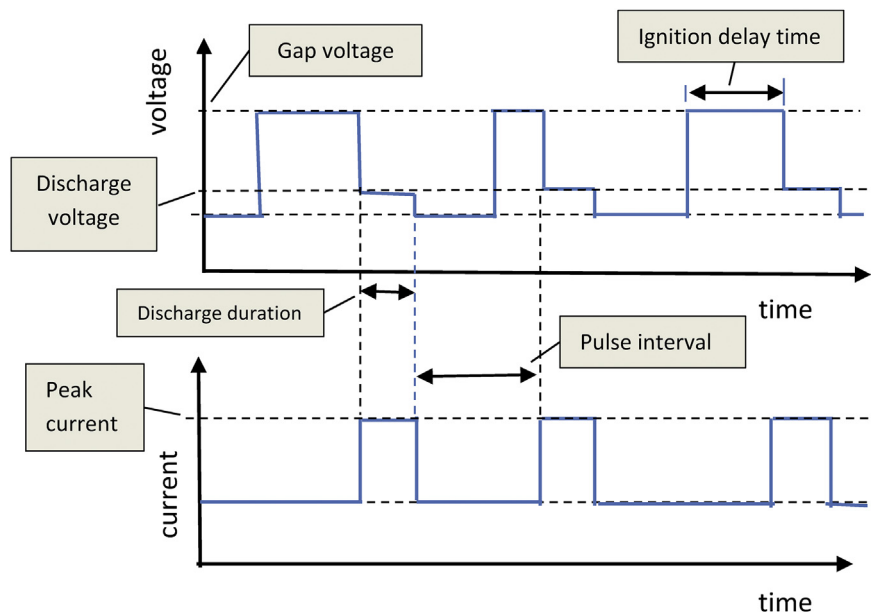
Figure 1. Schematic of electrical discharge pulses.

electrode surface. This will prevent from material removal. Therefore, in this case workpiece is connected to negative polarity for higher material removal rate compared to the tool electrode [29]. This explains higher material removal rate at electrodes that connected to negative polarity [31, 32, 33, 34, 35].

Although single discharge generates a single crater, series of pulses at random location develop overlapped craters and form a continuum coating of an alloyed layer on the workpiece surface. The intensity of discharge energy is critical to the formation of craters. An increase in the intensity can increase the depths and widths of craters, thus contributing to a high material removal and significant surface roughness [29, 36, 37, 38, 39]. Moreover, an implant with a high surface roughness can promote a suitable surface topography for an increase in the bone-implant contact, in addition to the enhancement of the bone ingrowth [40]. Y. Wang, et al. [41] reported that the oxide formation under EDC process can develop significant bone-like apatite after 7-days of simulated body fluid (SBF) immersion.

Based on the abovementioned reviews, the aim of this study was the comprehensive investigation of the effects of the EDC parameters with respect to the recast layer thickness, surface roughness, and single crater formation on the NiTi alloy using deionized water as the dielectric fluid in the EDC process. The deionized water is an important medium to develop an oxide surface layer through the recast formation from the composition of molten electrode and H_2O molecules breakdown. The deionized water can increase the oxygen concentration in the process environment, thus increase the stoichiometric composition of the titanium surface oxide, and reduce the migration of nickel into the recast layer. Thus, more potential of titanium oxide layer from the recast layer formation can be developed on the NiTi surface with respect to the condition of the EDC parameters. In additional, the measurement data with respect to the chemical composition, surface topography, and temperature transformation of the EDC substrates are presented to supplement the main findings of this study.

2. Materials and methods

2.1. Machine, material, and preparation

In this work, EA8 Mitsubishi Die Sinker machine was used. X, Y, and Z-axes travel dimensions are 300 mm × 250 mm × 250 mm in the, respectively. The machine has an internal circulation system that can contain a maximum of 250 L of dielectric fluid. The material substrate is made of a medical grade nickel-titanium alloy (NiTi) shape memory alloy in accordance with the ASTM F2063-12 standard, with dimensions of 70 mm × 70 mm × 5 mm. The chemical composition, mechanical properties, and thermal transformation of the alloy are shown in Table 1. The tool electrode for the EDC process was a Grade II pure titanium rod (99.99% purity) with dimensions of Ø10 mm × 8 mm. The tool attached on a pure titanium rod with dimensions of Ø10 mm × 50 mm using a copper adhesive film, and fixed at a tool holder.

Upon the completion of the EDC process, the surfaces of the material substrates were prepared via the metallographic method. The substrates

were ground sequentially using SiC abrasive paper with grit sizes of 180, 400, 800, 1000, and 2000 until the mirror finish was obtained. The surface was then polished using a polishing cloth with a monocrystalline diamond suspension and etched using Kroll's reagent formulation for 10 s. These steps were applied to the tool electrode and cross-sectional substrates for the measurement of the recast layer thickness.

2.2. Experimental design

A two-level full factorial design was employed to layout the experiment. Five parameters were varied as shown in Table 2. The total number of trials was 38 including six centre points runs. The software generated analysis of variance (ANOVA) table was used to identify the significant parameters with respect to the outcomes of the recast layer thickness, crater sizes, and surface roughness. Based on the ANOVA, the significant findings with respect to the main effects of parameters or interactions among them were reported when their probability of being wrong (p-value) less than 0.05.

2.3. Experimental setup and measurement

Figure 2 presents an image of the experimental setup. The trials were conducted in a carbon steel reservoir, which was fixed on the EDM machine table. The reservoir was filled with 200 ml of deionized water as the dielectric fluid. To display and monitor the waveforms in each trial, voltage and current sensors were attached to the reservoir and electrode, which was linked to an RTO1014 R&S oscilloscope with a bandwidth of 1
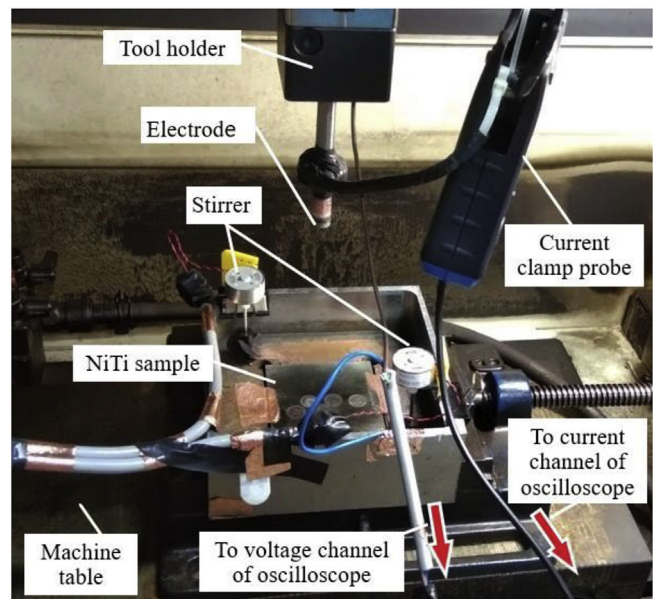
Figure 2. Photograph image of the experimental setup.

Table 1. Composition of NiTi sample, mechanical properties and temperature transformation.

Chemical composition (%):

Ni	Ti	C	O	N	H	Co	Cu	Cr	Nb	Fe
55.6	44.297	0.045	0.03	0.003	0.002	0.005	0.005	0.006	0.005	0.002

Mechanical properties and temperature transformation:

Tensile strength			Elongation				Yield strength
850 MPa			16%				202 MPa

Martensite Start Temperature	Martensite Finish Temperature	Austenite Start Temperature	Austenite Finish Temperature
-6.02 °C	-27.79 °C	16.14 °C	25.16 °C

Table 2. Experimental conditions.

No	Parameters	Unit	Condition
1	Polarity	-	straight (-), reverse (+)
2	Discharge duration	μs	50,540
3	Pulse interval	ms	6,8
4	Peak current	A	3,9
5	Gap voltage	V	80,260
6	Jump function	-	off
7	Electrode type	-	10 mm dia. pure titanium
8	Dielectric fluid	-	200 ml of deionized water
9	Machining time	min.	90 min

GHz and acquisition rate of 10 Gsample/s. The machining period of each trial was set as 30 s and 90 min, for the development of single craters and a recast layer, respectively.

The measurement data of the single crater and recast layer thickness were obtained from the images captured using an Xoptron X80 series optical microscope at magnifications of 500× and 1000×. Prior to the measurement of the recast layer thickness, the metallographic method was applied to the cross-sectioned substrates, as previously detailed. Thereafter, 40 thickness measurements were conducted at different positions along the deposition surface. Moreover, the roughness of the substrates was determined with respect to the arithmetic average Ra using a Handysurf E-35B tester. The cut-off length of the measurement was 0.8 mm, with sampling lengths of 4.0 mm. The x-ray Diffraction (XRD) profiles of the modified substrates were obtained using a Bruker D2 Phaser. The XRD tester was equipped with LYNXEYE detectors based on Cu-Kα radiation. The scanning rate was 0.1 s/step within a scanning range of 10–100°. To support the previous experimental data, several selected cross-sectioned sample images and surface topographies were captured using scanning electron microscopy (SEM; JEOL JSM-6010LV) at magnifications of 1000× and 500×, respectively. Thereafter, the thermal and phase transformations of the substrates due to the EDC process were examined using a TA Q20 differential scanning calorimetry (DSC) instrument. The cooling and heating rates were 10 °C/min, and the temperature ramp was between -60 °C and 70 °C. Selected samples were used for this measurement.

3. Results and discussion

All the measurements conducted on the coated NiTi surface, which included the recast layer thickness, crater sizes, and average surface roughness (Ra), are shown in Table 3.

3.1. Recast layer formation

In general, the quality aspect of the recast layer formation is determined based on the measurement of the recast layer thickness and crater sizes. Formation of each crater is the basis for surface coatings in the EDC process, and its characteristics are determined by power density of each discharge. Repetitive discharges on the material surface were found to develop a continuum coating with a new chemical composition, comprising the elements from the dielectric fluid, electrode material, and substrate material. Based on the experimental results, the XRD profiles of the material deposition are shown in Figure 3. Compared with the unmodified substrate, an additional chemical composition of titanium oxide (TiO) was observed on the NiTi substrate after the coating process under low operating parameters. Moreover, Figure 4 presents the SEM images of the oxide layer formation on the modified substrates. Based on a comparison of the operating conditions shown in Figure 4a(i), b(i), the thickness of the oxide layer was found to increase in accordance with an increase in the discharge duration. No folding features were observed in Figure 4b(ii); which is different from the case with the low operating

parameters, as shown in Figure 4a(ii). However, porosities were observed on the surfaces connected to the parent material, which are unfavourable, as they lead to the exposure of the NiTi surface to the environment.

Under low operating parameters, voids developed on the surface due to the gas bubbles, which were released during the EDC process, as shown in Figure 4a(ii). Moreover, microcracks were observed on the EDC

(a)

(b)
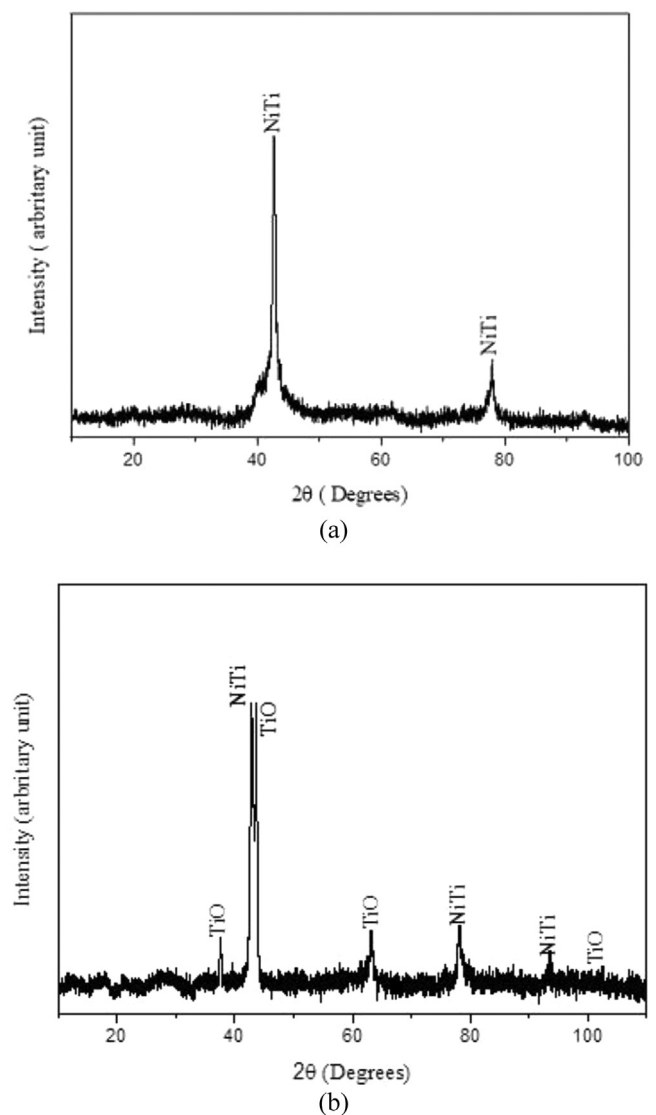
Figure 3. X-Ray Diffraction profiles of (a) NiTi alloy, (b) Low working condition of EDC substrate.

surface under the low operating parameters, which was different from the case at high discharge durations. Microcracks were formed due to thermal stresses, which can be attributed to cooling of recast layer due to discharges [23, 42]. An increase in the discharge duration can increase the heat energy and thermal stress. However, the abovementioned operating conditions indicate an excessive generation of debris particles, which contribute to a higher deposition, especially in the microcrack regions. Moreover, the particles decreased the thermal shock on the modified surface due to the increase in the discharge gap size [27].

The analyses of the recast layer thickness, crater size, and average surface roughness are summarised in Figure 5. The bar chart indicates that all the performance measures are dependent on the discharge duration. This parameter was found to have an influence on the discharge energy per unit time per unit cross sectional area of the discharge column, so-called power density. In particular, higher power density will increase ratio of total removal volume per pulse with respect to the molten area volume, so-called removal efficiency, R_e [43]. Furthermore, in the case of Sinking EDM, R_e is between 1 and 10 %, which means at lower power density, more molten area remains at the crater [44]. Thus, high thermal energy generated on the substrate at long discharge duration, will increase the amount of molten material in the discharge gap.

Moreover, the statistical analyses indicated that the polarity, discharge duration, and peak current have a significant influence on the recast layer thickness as also shown in the ANOVA table, Table 4. The influence of these parameters on the recast layer thickness is shown in Figure 6. The figure indicates that the layer thickness increased with an increase in the discharge duration and peak current. However, the discharge duration exhibited a higher tendency to increase the material deposition than the peak current. A high discharge energy also was found to increase the temperature of the discharge column and promote oxygen absorption to the molten material [29]. Thus, the higher oxygen absorption increased the thickness of the oxide layer on the substrate surface. Furthermore, a higher generation of discharge energy due to the high level of discharge duration and peak current increase the amount of molten material and small debris that are suspended in the deionized water. Instead of molten material, the suspended debris also participate in the formation of recast layer. The debris was the evaporated material during discharging that solidifies because of the sudden drop of pressure after the plasma channel collapses [45]. During a new pulse, the suspended debris melted by the high temperature of the plasma channel, and then moved and attached on the substrate surface. Moreover, the debris also involved in decreasing the microcracks on the recast layer surface as shown in Figure 4. Even

Table 3. Set of process conditions and measurement results under full factorial design.

Std.no.	Polarity	Discharge duration (μs)	Pulse interval (ms)	Peak current (A)	Gap voltage (V)	Recast layer thickness (μm)	Crater size (μm)	Ra (μm)
1	-	50	6	3	80	4.39	78.83	1.92
2	+	50	6	3	80	2.09	62.26	2.99
3	-	540	6	3	80	19.53	258.26	5.67
4	+	540	6	3	80	15.79	424.88	5.42
5	-	50	8	3	80	2.42	77.51	2.75
6	+	50	8	3	80	2.22	66.94	3.35
7	-	540	8	3	80	20.28	353.06	5.11
8	+	540	8	3	80	12.94	192.95	5.05
9	-	50	6	9	80	7.84	109.51	3.31
10	+	50	6	9	80	2.10	112.44	3.60
11	-	540	6	9	80	21.89	559.51	5.92
12	+	540	6	9	80	16.40	657.59	6.02
13	-	50	8	9	80	11.22	100.99	3.26
14	+	50	8	9	80	2.79	218.63	4.09
15	-	540	8	9	80	13.73	455.28	6.01
16	+	540	8	9	80	14.59	543.18	6.28
17	-	50	6	3	260	2.21	71.36	1.58
18	+	50	6	3	260	2.53	77.25	2.12
19	-	540	6	3	260	16.72	242.55	4.45
20	+	540	6	3	260	16.81	258.68	4.96
21	-	50	8	3	260	3.01	79.53	1.34
22	+	50	8	3	260	2.30	86.59	1.87
23	-	540	8	3	260	17.10	197.44	5.27
24	+	540	8	3	260	14.69	276.55	4.42
25	-	50	6	9	260	4.62	104.35	1.90
26	+	50	6	9	260	6.61	103.37	3.26
27	-	540	6	9	260	22.47	446.83	7.02
28	+	540	6	9	260	14.10	498.06	5.68
29	-	50	8	9	260	3.10	125.15	1.98
30	+	50	8	9	260	1.85	103.90	2.20
31	-	540	8	9	260	14.44	451.53	7.06
32	+	540	8	9	260	17.54	480.20	6.06
33	-	295	7	6	170	9.38	236.40	3.05
34	+	295	7	6	170	6.37	179.28	3.09
35	-	295	7	6	170	9.80	187.99	2.64
36	+	295	7	6	170	7.04	168.59	2.98
37	-	295	7	6	170	8.60	197.28	2.71
38	+	295	7	6	170	5.12	238.25	2.73
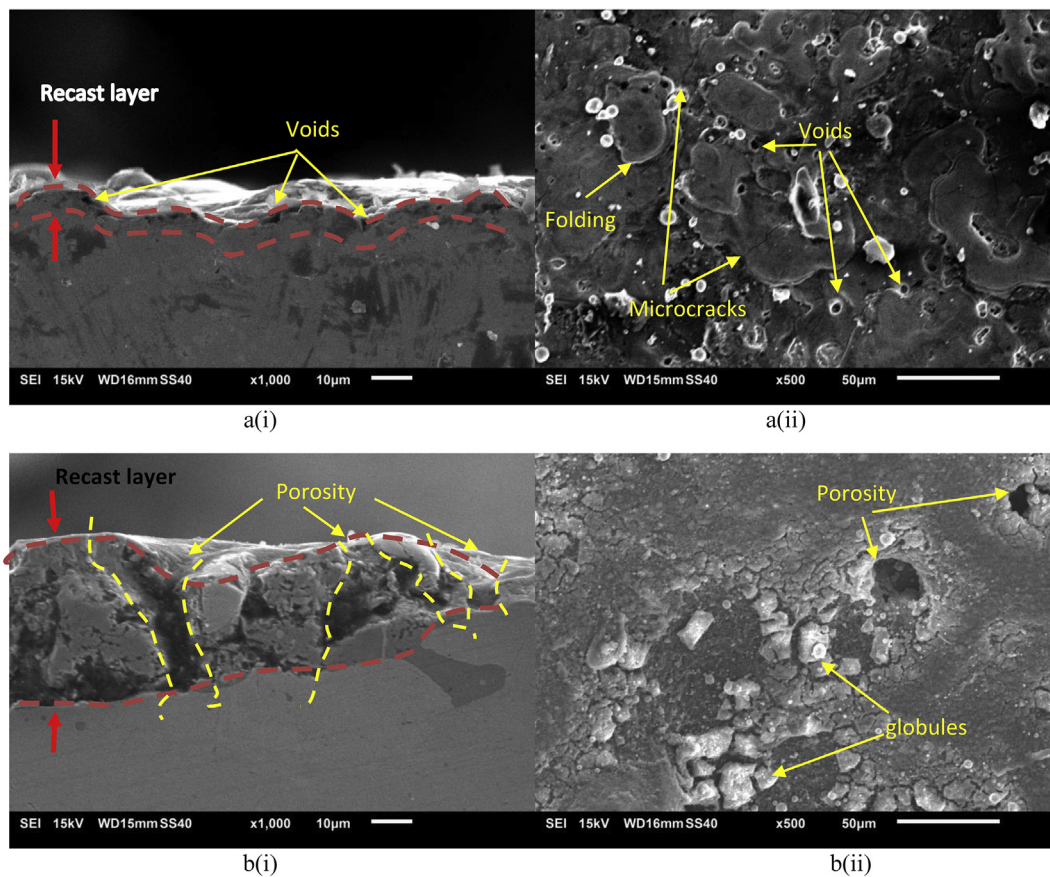
Figure 4. SEM images of (i) cross-sectioned and (ii) surface topography under; (a) Low working condition, (b) High discharge duration.
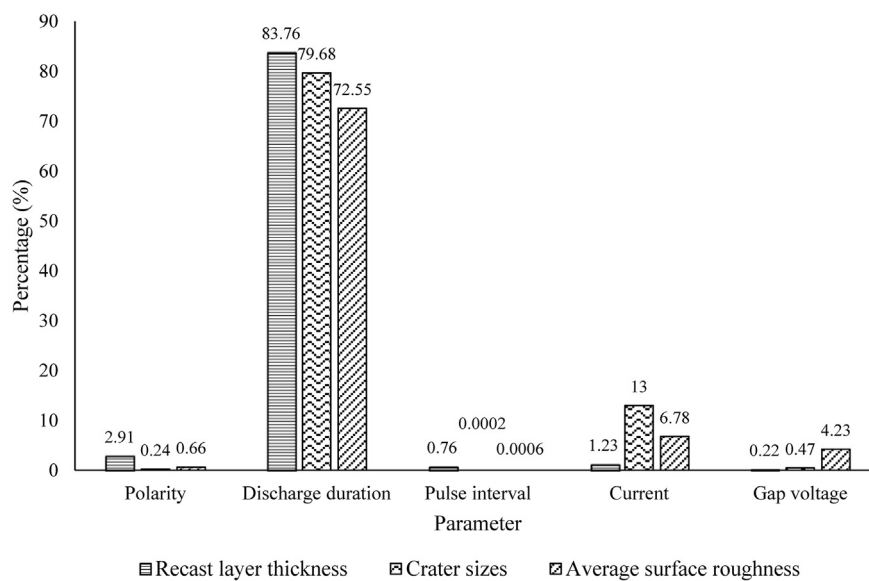
Performance measures	Polarity	Discharge duration	Pulse interval	Current	Gap voltage
Recast layer thickness	significant	significant	x	significant	x
Crater sizes	x	significant	x	significant	x
Avg. surface roughness	x	significant	x	significant	significant

Figure 5. Percentage contribution of parameters with significant justification to recast layer thickness, crater sizes and average surface roughness.

Table 4. ANOVA of recast layer thickness.

Source	Sum of Square	df	Mean Square	F-Value	p-value Prob > F
Model	42.75	6	7.13	57.01	<0.0001
A-Polarity	1.36	1	1.36	10.86	0.0026
B-Discharge duration	39.08	1	39.08	312.66	<0.0001
D-Peak current	0.57	1	0.57	4.59	0.0407
E-Gap voltage	0.10	1	0.10	0.80	0.3777
AE	0.67	1	0.67	5.37	0.0278
BD	0.53	1	0.53	4.23	0.0488
Curvature	0.27	2	0.14	1.10	0.3475
Residual	3.62	29	0.12		
Lack of fit	3.53	25	0.14	5.67	0.0515
Pure error	0.099	4	0.025		
Cor total	46.65	37			
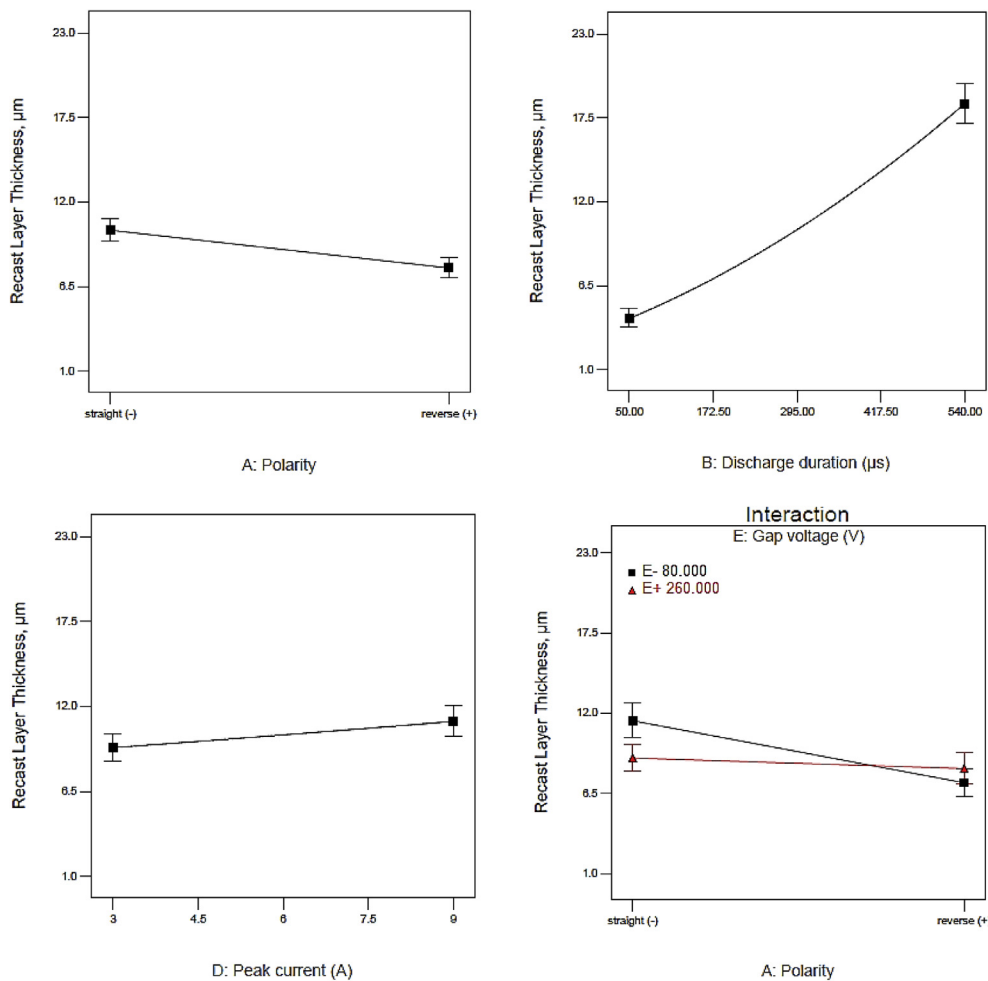
Figure 6. Model graphs of significant factors on recast layer thickness.

though at high discharge energy, the microcracks was invisible under the microscopy observation compared with low condition of discharge duration. Therefore, the debris formation is important in EDC process in order to sustain the quality of the recast layer.

The polarity was also found to be significant to the recast layer thickness. A higher layer thickness was recorded during the straight polarity when compared with the reverse polarity. However, the contribution of the polarity was minimal (approximately 2.91%) when compared with that of other electrical parameters (discharge duration and peak current). The recast layer thickness was marginally increased

with the straight polarity due to the higher material removal rate on the substrate. This was due to the difference in the energy dissipation on the positive and negative electrodes. There was a higher energy transfer on the positive electrode due to the higher flow of electrons than anions. Moreover, this was differentiated by the smaller mass of electrons when compared with that of the anions [25]. The migration of the titanium material from the solid electrode was not dependent on the formation of the recast layer. This can be verified by the results of the additional analyses of the material losses on the tool electrodes, as shown in Figure 7, which indicated that only 2.34 percent of the polarity

contributed to the material losses; thus confirming its lack of influence on the response.

3.2. Crater sizes

The ANOVA table as shown in Table 5 indicates the model is significant that acceptable for further prediction. The lack of fit is insignificant that implies the data is sufficiently fitted. The effect of the parameters to the craters sizes, as shown in Figure 5, indicate that the discharge duration was the most significant parameter with respect to the formation of craters. In particular, it contributed a maximum of 80%, followed by the peak current at 13%. In general, the model graph shown in Figure 8 indicates that both significant parameters exhibited positive effects on the crater sizes. According to S. Hsieh et al., the discharge duration and peak current mainly determine the discharge energy for the spark generation [26]. Thus, an increase in both parameters can significantly intensify the localised heat energy. The increase in the discharge duration resulted in an increase in the plasma diameter due to an increase in the duration of current flow. The increase in the plasma channel decreased the discharge energy per unit area and resulted in the formation of shallower craters, which increased the re-solidification rate of the molten material on the substrate surface [46].

Figure 9 presents the optical images of the single crater with respect to different parameter conditions. The images reveal the variations in the shapes and sizes of the formed craters. The reverse polarity condition (Figure 9(b)) resulted in the development of a bowl-shaped crater with a smaller size when compared with that of the straight polarity (see Figure 9(a)). T. Tamura et al. [47] reported that the crater shapes are significantly dependent on the polarity. Under the straight polarity conditions (Figures 9(a), (c)–(f)), shallow concave shapes with bulging rims were developed. The bulging rims were formed due to the molecular movement of the molten material, which caused the gas bubbles to
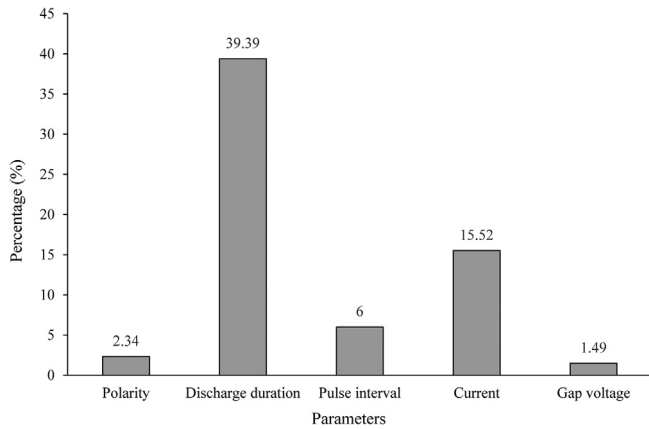
Figure 7. Percentage contribution of parameters to the material losses of tool electrodes.
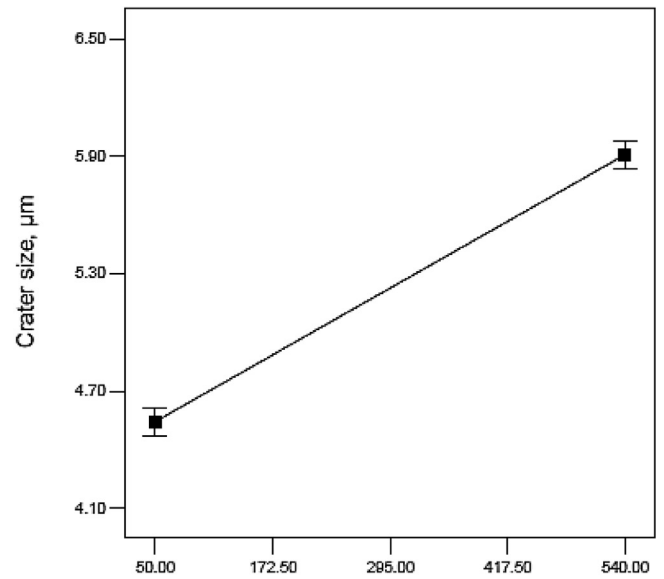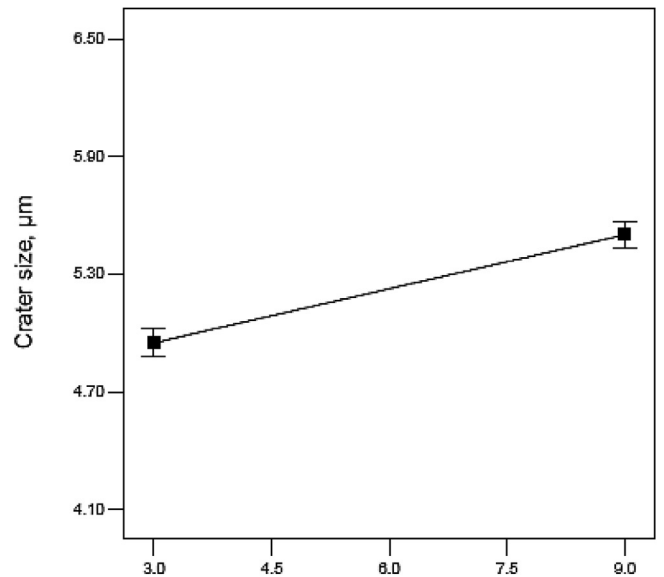
Figure 8. Model graphs of significant factors on crater sizes.

Table 5. ANOVA of crater size.

Source	Sum of Square	df	Mean Square	F-Value	p-value Prob > F
Model	0.024	2	0.012	227.42	<0.0001
B-Discharge duration	0.021	1	0.021	393.19	<0.0001
D-Peak current	3.28×10^{-3}	1	3.28×10^{-3}	61.64	<0.0001
Curvature	3.099×10^{-4}	2	1.55×10^{-4}	2.91	0.0684
Residual	1.756×10^{-4}	33	5.32×10^{-5}		
Lack of fit	1.637×10^{-3}	29	5.645×10^{-5}	1.90	0.2825
Pure error	1.187×10^{-4}	4	2.969×10^{-5}		
Cor total	0.026	37			

(a) Low condition

(b) Reverse polarity

(c) High discharge duration

(d) High pulse interval

(e) High current

(f) High gap voltage
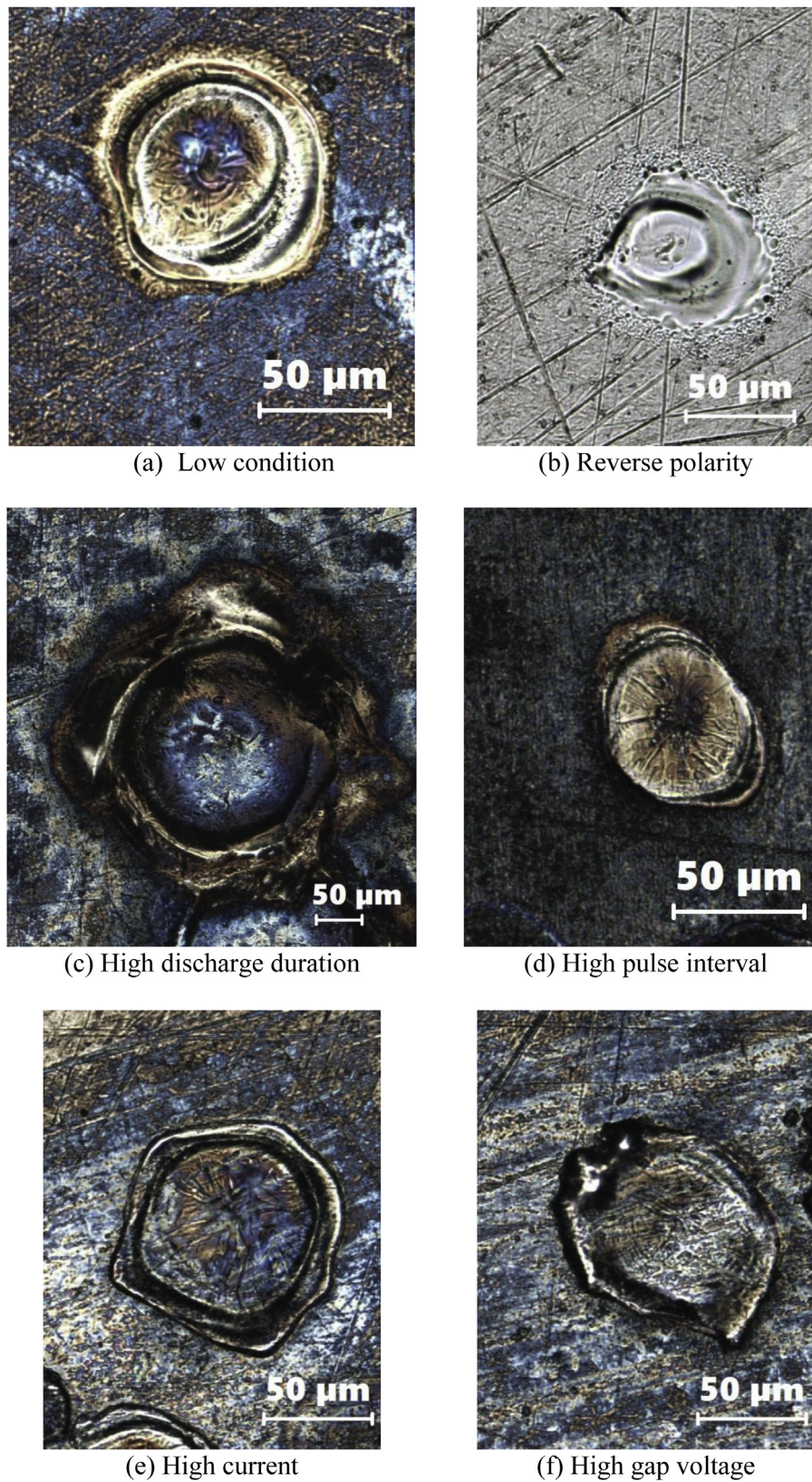
Figure 9. Optical images of single crater formation under different working conditions.

collapse at the end of each pulse, as detailed by X. Feng et al. [48]. The molecular movement was due to the impulsive force on the molten material [49]. In the case of the high discharge duration, a significantly large-sized crater was formed, as shown in Figure 9(c). Due to the long discharge time, the plasma diameter was larger, which resulted in a significant increase in the impulsive force [50]. Consequently, an

increased amount of molten material was extruded from the melt pool of the crater.

3.3. Average surface roughness

The ANOVA table of the average surface roughness (Ra) is presented in Table 6. The F-value of the model and the lack of fit are appropriate for further prediction. The influence of the EDC parameters on the surface roughness is shown in Figure 5, in which the discharge duration, peak current, and gap voltage had a significant influence on the surface roughness. Based on comparison of the abovementioned parameters, the discharge duration exhibited the highest contribution of up to 73%, followed by the peak current and gap voltage at 6.8% and 4.2%, respectively. The results are similar to those of the crater sizes, as described in Section 3.2. Moreover, a direct relationship was found between the critical parameters and influence of the discharge duration and peak current. The surface irregularities are dependent on the correlation between the crater size formation and discharge energy. In particular, surface irregularities were formed on the modified substrate due to the presence of numerous globules, which have attributed to the formation of a larger plasma channel, as discussed by K.L. Wu, et al. [51].

Figure 10 indicates that a rough surface was developed in accordance with an increase in the discharge duration and peak current. This corresponds to Ra $= C(I_p \ x \ \tau_p)^\beta$, where C and β are constants due to the mechanical and thermal properties, I_p = peak current, and τ_p = pulse duration; as theoretically detailed by T.S. Huang, et al. [17]. Conversely, an inverse relationship was found between the gap voltage and Ra. The gap voltage was found to have an influence on the gap distance between the electrode and substrate surface. The increase in the gap distance was due to the higher gap voltage, which decreased the effect of the sparking generation on the substrate surface. This result was confirmed by the formation of a single crater, as discussed in Section 3.2, which demonstrated the reduction in the crater size in accordance with an increase in the gap voltage. However, the effect of the gap voltage was mitigated in the case of a high discharge duration, as demonstrated by the curve of the discharge duration with respect to the gap voltage (Figure 10). Due to the increase in the discharge duration, the gap distance did not have a significant influence on the material erosion; thus, the surface deterioration was inhibited. Moreover, a similar trend was observed during the polarity shift. The reverse polarity resulted in a higher surface roughness than the straight polarity in the case of the short discharge duration. However, in the case of the longer discharge duration, a relatively constant surface roughness was observed. This can be attributed to the difference in the energy distribution between the electrode and substrate at high discharge durations, based on the T-F electron emission theory [52].

This theory states that due to the significance of both parameters (polarity and discharge duration), the emissions of the electrons and ions are significantly dependent on both parameters, thus resulting in a more constant effect.

Table 7 presents the model equations of all responses that are generated by regression modelling. The equations are in the transformation of square root and inverse square root in order to generate the normality of the data by selecting the best lambda value. The equations of recast layer thickness and average surface roughness (Ra) are differentiated based on the condition of the polarity, see Eqs. (2), (3), (4), and (5). Since the polarity is insignificant to the crater size, the parameter is discarded from the model equation as shown in Eq. (6).

3.4. Temperatures transformation

Figure 11 presents a comparison between the DSC curve of the unmodified NiTi under the low operating parameters of the EDC process and under high discharge durations. A rhombohedral phase (R-phase) was observed in the curves during the cooling stage due to the higher nickel concentration of the alloy. The curve also exhibited a completely austenite phase of the alloy at room temperature. Under the low operating parameters of the EDC process, the temperatures of the martensite start (M_s), martensite finish (M_f), austenite start (A_s), and austenite finish (A_f) decreased to -12.16 °C, -32.63 °C, 15.05 °C, and 23.19 °C from the initial temperatures of -6.02 °C, -27.79 °C, 16.14 °C, and 25.16 °C of the unmodified NiTi, respectively. The latent heat of the martensite (exothermic) and austenite (endothermic) phases slightly increased to 6.97 Jg^{-1} and 15.36 Jg^{-1} from 5.97 Jg^{-1} and 14.06 Jg^{-1} of the unmodified NiTi, respectively. Moreover, there were slight variations in the transformation temperature and latent heat after the EDC process due to the influence of the thermal energy on the morphology of the phases.

In the case of the high discharge duration, M_s, M_f, and A_f slightly decreased to -7.22 °C, -27.46 °C, and 24.47 °C, respectively; and A_s slightly increased to 16.58 °C. However, the latent heat of the martensite and austenite phases significantly increased to 8.32 Jg^{-1} and 17.19 Jg^{-1}, respectively. The martensite and austenite peak temperatures (M_p and M_p) were recorded at -16.24 °C and 21.23 °C, which were almost constant when compared with those of the unmodified substrate (-15.17 °C and 21.38 °C). Based on a comparison between the DSC curves, the temperature transformations of the martensite and austenite phases were observed in the EDC substrates. This can be attributed to the oxidation and alteration of the phase morphology due to the EDC process. Moreover, A_f of the substrate was less than the average human body temperature (37 °C). Hence, this is suitable for biomedical im-

Table 6. ANOVA of average surface roughness (Ra).

Source	Sum of Square	df	Mean Square	F-Value	p-value Prob > F
Model	6.03	6	1.01	114.10	<0.0001
A-Polarity	0.044	1	0.044	5.03	0.0327
B-Discharge duration	4.87	1	4.87	552.64	<0.0001
D-Peak current	0.46	1	0.46	51.63	<0.0001
E-Gap voltage	0.28	1	0.28	32.18	<0.0001
AB	0.16	1	0.16	17.92	0.0002
BE	0.22	1	0.22	25.08	<0.0001
Curvature	0.42	2	0.21	24.06	<0.0001
Residual	0.26	29	8.81×10^{-3}		
Lack of fit	0.24	25	9.648×10^{-3}	2.68	0.1748
Pure error	0.014	4	3.605×10^{-3}		
Cor total	6.71	37			
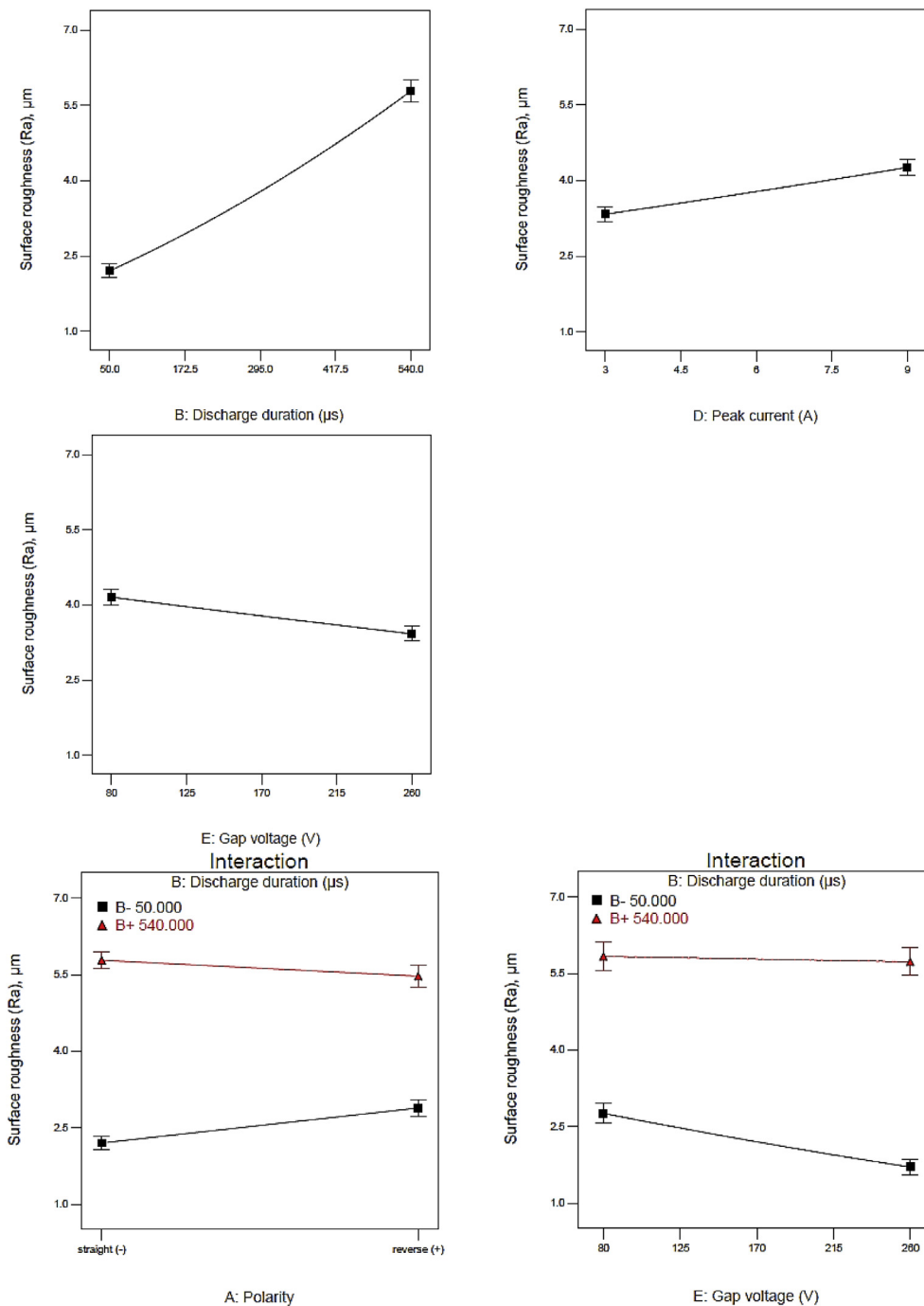
Figure 10. Model graphs of significant factors on average surface roughness (Ra).

plants, given that it can adequately sustain the shape memory effect within the temperature range of the intended application.

4. Conclusions

This paper presents the investigation of the effects of EDC parameters on the recast layer formation, crater sizes, and surface roughness of the NiTi shape memory alloy. Based on the results, the following conclusions were made.

- Based on ANOVA, the discharge duration was found to contribute most significantly to the formation of the recast layer, crater sizes, and

surface roughness, followed by the peak current. The above-mentioned parameters were found to have a significant effect on the discharge power density, thus influencing the material erosion, deposition, and surface structure.

- The polarity of the electrode was found to have a significant influence on the recast layer formation, and a slight influence on the crater sizes and surface roughness. Moreover, it was found to have a significant influence on the different energy dissipation between the tool electrode and the substrate.

- Besides, the gap voltage is critical to the variation formation of the crater sizes and surface roughness due to the influence of the gap distance with respect to the discharge density on the substrate surface.

Table 7. Model equations of the responses.

Condition	Model equation	Eq.
Straight polarity	Recast layer thickness, $\mu m =$ $[1.66 + (5.56 \times 10^{-3})(Discharge\ duration) + 0.10\ (Peak\ current) - (2.23 \times 10^{-3})(Gap\ voltage) - (1.75 \times 10^{-4})(Discharge\ duration)(Peak\ current)]^2$	(2)
	Average surface roughness(Ra), $\mu m =$ $[1.52 + (1.24 \times 10^{-3})(Discharge\ duration) + 0.04(Peak\ current) - (2.16 \times 10^{-3})(Gap\ voltage) + (3.77 \times 10^{-6})(Discharge\ duration)(Gap\ voltage)]^2$	(3)
Reverse polarity	Recast layer thickness, $\mu m =$ $[0.70 + (5.56x10^{-3})(Discharge\ duration) + 0.10(Peak\ current) + (9.87 \times 10^{-4})(Gap\ voltage) - (1.75 \times 10^{-5})(Discharge\ duration)(Peak\ current)]^2$	(4)
	Average surface roughness(Ra), $\mu m =$ $[1.76 + (6.65 \times 10^{-4})(Discharge\ duration) + 0.04(Peak\ current) - (2.16 \times 10^{-3})(Gap\ voltage) + (3.77 \times 10^{-6})(Discharge\ duration)(Gap\ voltage)]^2$	(5)
	$Crater\ size, \mu m = \left\{ \dfrac{1}{[0.13 - (1.04 \times 10^{-4})(Discharge\ duration) - (3.37 \times 10^{-3})(Peak\ current)]} \right\}^2$	(6)
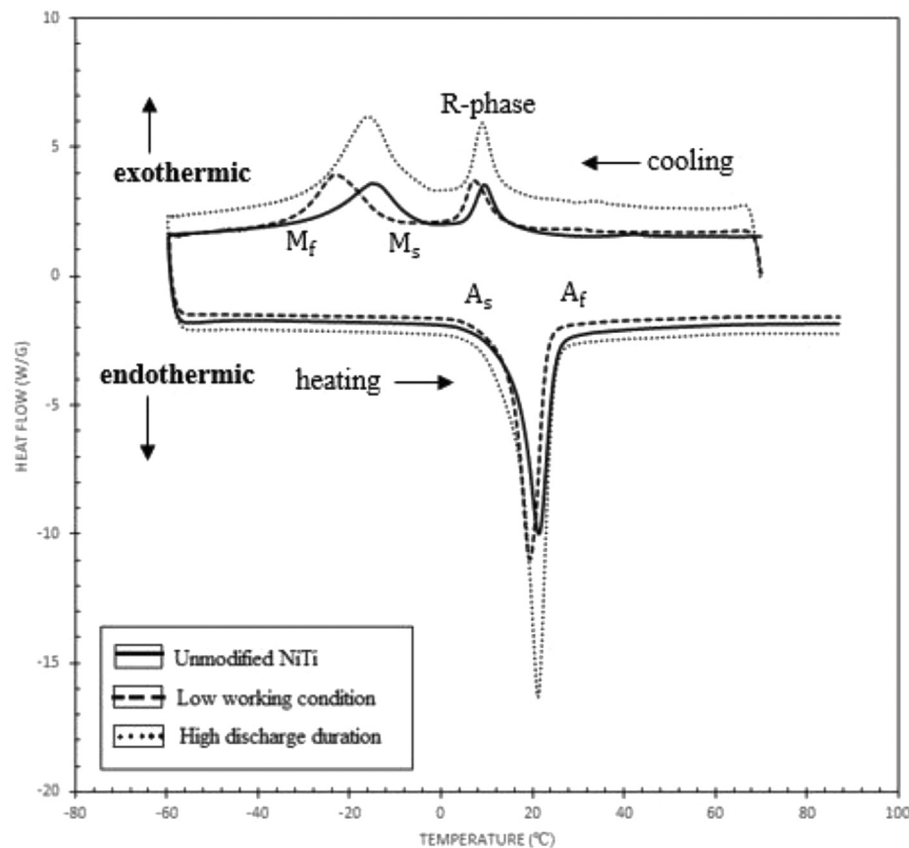
Figure 11. DSC curves of unmodified NiTi, low working condition and high discharge duration.

- The recast layer formation and surface roughness of the EDC substrate has a direct relationship with the crater formation, which was under the influence of the discharge power density.
- Several defects were observed on the EDC subtracts due to the effect of heat generation and the manner of material deposition. Further investigation is required to determine the feasibility of the EDC technique with respect to the application of coatings, and especially biomaterials.
- No significant temperature transformation was observed on the NiTi substrate under the low operating conditions and high discharge durations, especially with respect to the A_f temperature. Thus, the EDC process can sustain an adequate shape memory effect for biomedical applications.
- The presence of the microcracks and porosities on the coatings layer affected the performance of the recast layer formation as the nickel barrier. Thus, further investigation is necessary to identify the amount of nickel release due to the defects and introduces additional procedure to the process in order to prevent the issue.
- The formation of debris during EDC process can be further investigated in order to enhance the surface quality of the substrate material.

Declarations

Author contribution statement

Ahmad Fairuz Mansor: Conceived and designed the experiments; Performed the experiments; Analyzed and interpreted the data; Wrote the paper.

Azwan Iskandar Azmi: Conceived and designed the experiments; Analyzed and interpreted the data; Wrote the paper.

Mohd Zahiruddin Md Zain: Analyzed and interpreted the data; Wrote the paper.

Roshalliza Jamaluddin: Contributed reagents, materials, analysis tools or data; Wrote the paper.

Competing interest statement

The authors declare no conflict of interest.

Additional information

No additional information is available for this paper.

References

[1] L. Petrini, F. Migliavacca, Biomedical applications of shape memory alloys, J. Metall. (2011) 1–15.

[2] A. Wadood, Brief overview on nitinol as biomaterial, Adv. Mater. Sci. Eng. (2016) 1–9. Article ID 4173138.

[3] R. Roth, S. Coemert, S. Burkhardt, K.S. Rodewald, T.C. Lueth, A process towards eliminating cytotoxicity by removal of surface contamination from electrical discharge machined nitinol, Procedia CIRP 89 (2020) 45–51.

[4] D. Kapoor, Nitinol for medical applications: a brief introduction to the properties and processing of nickel titanium shape memory alloys and their use in stents, Johns. Matthey Technol. Rev. 61 (1) (2017) 66–76.

[5] F. Auricchio, E. Boatti, M. Conti, SMA Biomedical Applications, 2015.

[6] W. Haider, N. Munroe, V. Tek, C. Pulletikurthi, P.K.S. Gill, S. Pandya, Surface modifications of nitinol, J. Long Term Eff. Med. Implants 19 (2) (2009) 113–122.

[7] S.A. Shabalovskaya, H. Tian, J.W. Anderegg, D.U. Schryvers, W.U. Carroll, J. Van Humbeeck, The influence of surface oxides on the distribution and release of nickel from Nitinol wires, Biomaterials 30 (4) (2009) 468–477.

[8] A. Balamurugan, S. Rajeswari, G. Balossier, A.H.S. Rebelo, J.M.F. Ferreira, Corrosion aspects of metallic implants - an overview, Mater. Corros. 59 (11) (2008) 855–869.

[9] S.A. Shabalovskaya, G.C. Rondelli, A.L. Undisz, J.W. Anderegg, T.D. Burleigh, M.E. Rettenmayr, The electrochemical characteristics of native Nitinol surfaces, Biomaterials 30 (22) (2009) 3662–3671.

[10] X. Liu, P.K. Chu, C. Ding, Surface modification of titanium, titanium alloys, and related materials for biomedical applications, Mater. Sci. Eng. R Rep. 47 (3–4) (2004) 49–121.

[11] P.W. Peng, K.L. Ou, H.C. Lin, Y.N. Pan, C.H. Wang, Effect of electrical-discharging on formation of nanoporous biocompatible layer on titanium, J. Alloys Compd. 492 (1–2) (2010) 625–630.

[12] H.Q. Nguyen, D.A. Deporter, R.M. Pilliar, N. Valiquette, R. Yakubovich, The effect of sol-gel-formed calcium phosphate coatings on bone ingrowth and osteoconductivity of porous-surfaced Ti alloy implants, Biomaterials 25 (5) (2004) 865–876.

[13] A. Michiardi, C. Aparicio, J.A. Planell, F.J. Gil, New oxidation treatment of NiTi shape memory alloys to obtain Ni-free surfaces and to improve biocompatibility, J. Biomed. Mater. Res. B Appl. Biomater. 77 (2) (2006) 249–256.

[14] M. Pohl, T. Glogowski, C. Hessing, F. Unterumsberger, Formation of titanium oxide coatings on NiTi shape memory alloys by selective oxidation, Mater. Sci. Eng. A 482 (2008) 123–126.

[15] D.P. Aun, et al., Development of a flexible nanocomposite TiO2 film as a protective coating for bioapplications of superelastic NiTi alloys, Appl. Surf. Sci. 375 (2016) 42–49.

[16] N. Ohtsu, Y. Hirano, Growth of oxide layers on NiTi alloy surfaces through anodization in nitric acid electrolyte, Surf. Coatings Technol. 325 (2017) 75–80.

[17] T.-S. Huang, S.-F. Hsieh, S.-L. Chen, M.-H. Lin, S.-F. Ou, W.-T. Chang, Surface modification of TiNi-based shape memory alloys by dry electrical discharge machining, J. Mater. Process. Technol. 221 (2015) 279–284.

[18] P. Harcuba, L. Bačáková, J. Stráský, M. Bačáková, K. Novotná, M. Janeček, Surface treatment by electric discharge machining of Ti-6Al-4V alloy for potential application in orthopaedics, J. Mech. Behav. Biomed. Mater. 7 (2012) 96–105.

[19] C. Prakash, H.K. Kansal, B.S. Pabla, S. Puri, "Experimental investigations in powder mixed electric discharge machining of Ti–35Nb–7Ta–5Zrβ-titanium alloy, Mater. Manuf. Process. 32 (3) (2017) 274–285.

[20] T.T. Öpöz, H. Yaşar, N. Ekmekci, B. Ekmekci, Particle migration and surface modification on Ti6Al4V in SiC powder mixed electrical discharge machining, J. Manuf. Process. 31 (2018) 744–758.

[21] S.F. Ou, C.Y. Wang, Fabrication of a hydroxyapatite-containing coating on Ti-Ta alloy by electrical discharge coating and hydrothermal treatment, Surf. Coatings Technol. 302 (2016) 238–243.

[22] T. Chang-Bin, L. Dao-Xin, W. Zhan, G. Yang, Electro-spark alloying using graphite electrode on titanium alloy surface for biomedical applications, Appl. Surf. Sci. 257 (15) (2011) 6364–6371.

[23] B.E.J. Lee, S. Ho, G. Mestres, M. Karlsson Ott, P. Koshy, K. Grandfield, Dual-topography electrical discharge machining of titanium to improve biocompatibility, Surf. Coatings Technol. 296 (2016) 149–156.

[24] S. Abdulkareem, A. Ali Khan, M. Konneh, Cooling effect on electrode and process parameters in EDM, Mater. Manuf. Process. 25 (6) (2010) 462–466.

[25] M. Gostimirovic, P. Kovac, B. Skoric, M. Sekulic, Effect of electrical pulse parameters on the machining performance in EDM, Indian J. Eng. Mater. Sci. 18 (6) (2011) 411–415.

[26] S.F. Hsieh, M.H. Lin, S.L. Chen, S.F. Ou, T.S. Huang, X.Q. Zhou, Surface modification and machining of TiNi/TiNb-based alloys by electrical discharge machining, Int. J. Adv. Manuf. Technol. 86 (5–8) (2016) 1475–1485.

[27] H. Marashi, A.A.D. Sarhan, M. Hamdi, Employing Ti nano-powder dielectric to enhance surface characteristics in electrical discharge machining of AISI D2 steel, Appl. Surf. Sci. 357 (Dec. 2015) 892–907.

[28] K.S. Vinoth, K.M. Pradeep, Experimental investigation of the process parameters in cryogenic cooled electrode in EDM, J. Mech. Sci. Technol. 29 (9) (2015) 3865–3871.

[29] M. Kunieda, B. Lauwers, K.P. Rajurkar, B.M. Schumacher, Advancing EDM through fundamental insight into the process, CIRP Ann. Manuf. Technol. 54 (2) (2005) 64–87.

[30] S. Clijsters, K. Liu, D. Reynaerts, B. Lauwers, EDM technology and strategy development for the manufacturing of complex parts in SiSiC, J. Mater. Process. Technol. 210 (4) (2010) 631–641.

[31] S. Chakraborty, S. Kar, S.K. Ghosh, V. Dey, Parametric optimization of electric discharge coating on Aluminium-6351 alloy with green compact silicon carbide and copper tool: a Taguchi coupled utility concept approach, Surfaces Interfaces 7 (2017) 47–57. February.

[32] H. Xiao, X. Jie, Z. Zeng, G. Li, Titanium carbonitride coating by pulsed electrical discharge in an aqueous solution of ethanolamine, Surf. Coatings Technol. 258 (2014) 1006–1010.

[33] Y.F. Chen, H.M. Chow, Y.C. Lin, C.T. Lin, Surface modification using semi-sintered electrodes on electrical discharge machining, Int. J. Adv. Manuf. Technol. 36 (568) (2008) 490–500.

[34] S. Kar, S. Chakraborty, V. Dey, S.K. Ghosh, Optimization of surface roughness parameters of Al-6351 alloy in EDC process: a Taguchi coupled fuzzy logic approach, J. Inst. Eng. Ser. C (2016) 1–12.

[35] M. Hanif, W. Ahmad, S. Hussain, M. Jahanzaib, A.H. Shah, Investigating the effects of electric discharge machining parameters on material removal rate and surface roughness on AISI D2 steel using RSM-GRA integrated approach, Int. J. Adv. Manuf. Technol. 101 (5–8) (2019) 1255–1265.

[36] W. Theisen and A. Schuermann, "Electro discharge machining of nickel-titanium shape memory alloys," Mater. Sci. Eng. A, vol. 378, no. 1-2 SPEC. ISS., pp. 200–204, 2004.

[37] S.J. Algodi, et al., Electrical discharge coating of nanostructured TiC-Fe cermets on 304 stainless steel, Surf. Coatings Technol. 307 (2016) 639–649.

[38] S.R. Arunachalam, S.E. Galyon Dorman, R.T. Buckley, N.A. Conrad, S.A. Fawaz, Effect of electrical discharge machining on corrosion and corrosion fatigue behavior of aluminum alloys, Int. J. Fatigue 111 (2018) 44–53. January.

[39] A. Bhattacharya, A. Batish, G. Bhatt, Material transfer mechanism during magnetic field-assisted electric discharge machining of AISI D2, D3 and H13 die steel, Proc. Inst. Mech. Eng. Part B J. Eng. Manuf. 229 (1) (2015) 62–74.

[40] R. Krishna Alla, K. Ginjupalli, N. Upadhya, M. Shammas, R. Krishna Ravi, R. Sekhar, Surface roughness of implants: a review, Trends Biomater. Artif. Organs 25 (3) (2011) 112–118.

[41] Y.H. Wang, C.C. Liao, Y.C. Chen, S.F. Ou, C.Y. Chiu, The feasibility of eco-friendly electrical discharge machining for surface modification of Ti: a comparison study in surface properties, bioactivity, and cytocompatibility, Mater. Sci. Eng. C 108 (415) (2020) 110192.

[42] M. Zahiruddin, M. Kunieda, Analysis of micro fin deformation due to micro EDM, Procedia CIRP 42 (Isem Xviii) (2016) 569–574.

[43] M. Zahiruddin, M. Kunieda, Comparison of energy and removal efficiencies between micro and macro EDM, CIRP Ann. Manuf. Technol. 61 (1) (2012) 187–190.

[44] F. Van Dijck, Physico-mathematical Analysis of the Electr Discharge Machining Process, PhD Thesis, Cathol. Univ. Leuven, 1973.

[45] S.J. Algodi, A.T. Clare, P.D. Brown, Modelling of single spark interactions during electrical discharge coating, J. Mater. Process. Technol. 252 (2018) 760–772. May 2017.

[46] F.L. Amorim, V.A. Dalcin, P. Soares, L.A. Mendes, Surface modification of tool steel by electrical discharge machining with molybdenum powder mixed in dielectric fluid, Int. J. Adv. Manuf. Technol. 91 (1–4) (2017) 341–350.

[47] T. Tamura, Y. Kobayashi, Measurement of impulsive forces and crater formation in impulse discharge, J. Mater. Process. Technol. 149 (1–3) (2004) 212–216.

[48] X. Feng, Y.S. Wong, G.S. Hong, Characterization and geometric modeling of single and overlapping craters in micro-EDM, Mach. Sci. Technol. 20 (1) (2016) 79–98.

[49] Z. Liu, Investigation on the influence of the dielectrics on the material removal characteristics of EDM, J. Mater. Process. Technol. 214 (2014) 1052–1061. May.

[50] M. Zhang, Q. Zhang, G. Zhu, Q. Liu, J. Zhang, Effects of some process parameters on the impulse force in single pulsed EDM, Procedia CIRP 42 (Isem Xviii) (2016) 627–631.

[51] K.L. Wu, B.H. Yan, F.Y. Huang, S.C. Chen, Improvement of surface finish on SKD steel using electro-discharge machining with aluminum and surfactant added dielectric, Int. J. Mach. Tools Manuf. 45 (2005) 1195–1201.

[52] T.H. Lee, T-F theory of electron emission in high-current arcs, J. Appl. Phys. 30 (2) (1959) 166–171.